Journal of Hazardous Materials 217–218 (2012) 187–193

Contents lists available at SciVerse ScienceDirect

Journal of Hazardous Materials

journal homepage: www.elsevier.com/locate/jhazmat

Dissolution of explosive compounds TNT, RDX, and HMX under continuous flow conditions

Chao Wang[a], Mark E. Fuller[b], Charles Schaefer[b], Jeffrey L. Caplan[a,c], Yan Jin[a,*]

[a] Department of Plant and Soil Sciences, University of Delaware, Newark, DE 19716, USA
[b] Shaw Environmental, Inc., 17 Princess Road, Lawrenceville, NJ 08648, USA
[c] Delaware Biotechnology Institute, University of Delaware, Newark, DE 19716, USA

ARTICLE INFO

Article history:
Received 6 September 2011
Received in revised form 2 March 2012
Accepted 6 March 2012
Available online 16 March 2012

Keywords:
TNT
RDX
HMX
Dissolution
Mass transfer

ABSTRACT

2,4,6-trinitrotoluene (TNT), hexahydro-1,3,5-trinitro-1,3,5-triazine (RDX), and octahydro-1,3,5,7-tetranitro-1,3,5,7-tetrazocine (HMX) are common contaminants around active military firing ranges. Dissolution of these compounds is usually the first step prior to their spreading in subsurface environments. Nevertheless, dissolution of individual TNT, RDX, and HMX under continuous flow conditions has not been well investigated. This study applied spectral confocal microscopy to observe and quantify the dissolution of TNT, RDX, and HMX (<100 μm crystals) in micromodel channels. Dissolution models were developed to describe the changes of their radii, surface areas, volumes, and specific surface areas as a function of time. Results indicated that a model incorporating a resistance term that accounts for the surface area in direct contact with the channel surfaces (and hence, was not exposed to the flowing water) described the dissolution processes well. The model without the resistance term, however, could not capture the observed data at the late stage of TNT dissolution. The model-fitted mass transfer coefficients were in agreement with the previous reports. The study highlights the importance of including the resistance term in the dissolution model and illustrates the utility of the newly developed spectral imaging method for quantification of mass transfer of TNT, RDX, and HMX.

1. Introduction

Numerous site investigations have shown that TNT, RDX, and HMX are three of the most common contaminants around active military firing ranges [1]. These compounds are associated with harmful effects on the liver [2–4], and TNT and RDX were classified as potential human carcinogens [5]. The United States Environmental Protection Agency (USEPA) set the lifetime exposure drinking water health advisory limits of TNT, RDX, and HMX in 2006, which are 2, 2, and 400 μg/L, respectively [5].

The first step to the entry and spreading of these contaminants in subsurface environments is the dissolution of TNT, RDX, and HMX from the mixed solid-phase energetic residues [6–13], which have been distributed around military ranges after detonation events [6,14–19]. Residues dissolve through the direct impact of precipitation events, by flowing surface runoff, or by percolating soil pore water.

Previous studies on the dissolution of individual TNT, RDX, and HMX were mostly performed in batch systems [11,20–24]. Concentrations of the dissolved TNT, RDX, and HMX in batch systems generally increased as the dissolution process progressed, coming to an apparent stop when the concentrations reached their solubility limits. Valuable information has been obtained in batch systems, such as data that indicated that the solubility and dissolution rates of TNT, RDX, and HMX were not affected by pH in the range from 4.2 to 6.2 [21].

Nevertheless, dissolution of individual TNT, RDX, and HMX under flow conditions has not been extensively investigated [8,16], whereas additional information might still be available in regards to the behavior of their mixed energetic residues under flow conditions. In contrast to batch systems, concentrations of the dissolved TNT, RDX, and HMX under continuous flow conditions are usually low and remain well below the solubility limits. Investigations under such conditions are of interest because they more closely represent in situ field conditions.

The purpose of this study was to investigate the dissolution of individual TNT, RDX, and HMX crystals under continuous flow conditions. A newly developed spectral imaging method [25] was applied to visualize and quantify the dissolution of TNT, RDX, and HMX in glass micromodel channels. Such direct visualization and quantification complements batch and column studies by providing additional information into the pore-scale dissolution processes. Parameters describing individual particles (e.g., radii, surface areas, volumes, and specific surface areas) were measured

* Corresponding author. Tel.: +1 302 831 6962; fax: +1 302 831 0605.
E-mail address: yjin@udel.edu (Y. Jin).

0304-3894/$ – see front matter © 2012 Elsevier B.V. All rights reserved.
doi:10.1016/j.jhazmat.2012.03.012

throughout the dissolution processes, and dissolution models were developed and applied to describe the changes of those parameters as a function of time and to provide insights about the dissolution processes.

2. Materials and methods

2.1. TNT, RDX, and HMX

Particles of TNT (linear crystals, 100–1000 μm), RDX (oblong crystals, 10–100 μm), and HMX (oblong crystals, 5–50 μm) were obtained through the recrystallization from the respective saturated aqueous solutions, which were prepared with 99% pure compounds [10]. Representative transmission light (bright field) images of individual explosive crystals are shown in Fig. 1(a1) to (c1). The long linear TNT crystals were manually broken into smaller pieces for the micromodel dissolution experiments.

2.2. Micromodel experiments

Uncoated (hydrophobic), sterile IBIDI μ-slide VI glass chambers (AutoMate Scientific, Inc., Berkeley, CA) were used as the micromodel devices for the dissolution experiments. The experimental setup was similar to that described previously by Wang et al. [25]. Briefly, one of the six micromodel channels in a glass chamber was loaded with 40 μL of solution which contained TNT, RDX, or HMX crystals. The experimental solution, which was a synthetic rainwater/groundwater (pH 5 and ionic strength ~0.3 mM) as described elsewhere [25], was thereafter pumped through silicon tubing to the channel at the flow rate of 60 μL/min (equivalently 658 μm/s). Individual TNT, RDX, or HMX particle(s) that attached to the channel wall in the upstream region were observed under a Zeiss LSM 510 Meta confocal microscopy. Spectral images [25] of 3-dimensional (D) z-stacks over time (4-D) were subsequently captured using the Zeiss LSM 510 software (Version 4.2). The spectral images captured a full emission spectrum, i.e., emission intensity at the wavelengths from 411 to 754 nm, at every pixel of the 3-D images. Each dissolution experiment was replicated three times thereafter. Representative parameters and typical instrumental settings are summarized in Table S1.

It is worth noting that the flow rate used in the present study was high, mainly with the following considerations. First, the adopted flow rate allowed the dissolution to be observed in a reasonable time frame (~hours) by confocal microscopy. The data could thus be collected in relatively short time, unlike from those field experiments which usually lasted ~year. Second, the collected data could be used to test the model and meanwhile phenomena that would be observed might still occur at the low flow rate. Third, the obtained mass transfer coefficients at the high flow rate could be utilized further, together with others from the literature, to regress equations describing the dependence of mass transfer coefficient on flow rate as in our next planned publication.

2.3. Image analysis

The obtained spectral images were decomposed using the LSM 510 software (Version 4.2) with the linear unmixing method, which is the most common approach for decomposing spectral images [26,27]. The reference spectrum (or spectral signature) of TNT, RDX, or HMX that would be used during the linear unmixing processes was acquired prior to the dissolution experiments. The unmixed images were reconstructed into 3-D images to measure the parameters relevant to particles, i.e. volumes (μm^3) and surface areas (μm^2), using Volocity image analysis software (Version 4.1.0). The typical Volocity protocol used for image analysis was as follows [28]: segment objects based on intensity, fill holes in objects to remove internal holes, clip objects into a region of interest, and exclude objects by size to avoid measurement noise. The measured data were then processed to calculate the particle radii (μm), shape factors, masses (μg), and specific surface areas (m^2/g) with equations described in Section 3.

3. Dissolution models

3.1. Model based on Fick's Law

The individual particles of TNT, RDX, and HMX attached to the channel wall in the present study, with a portion of the particle in contact with the flowing water [Fig. S1(a)]. The particles also did not move significantly during the dissolution processes, indicating that attractive interactions (e.g., most likely hydrophobic attraction [25]) occurred between the particle and channel wall.

The geometry of the particle can be expressed as [28]

$$a = \frac{4\pi r^2}{S} \tag{1}$$

$$V = \frac{4}{3}\pi r^3 \tag{2}$$

where a is surface area (μm^2), r is radius (μm) of a perfect sphere that has spherical shape and smooth surface and also has the same volume as the real particle, S is shape factor (dimensionless) which is defined as the ratio of the surface area of the perfect sphere to that of the real particle, and V is particle volume (μm^3). The shape factors were assumed constant since their values were generally stable throughout the dissolution processes. Moreover, the shape factor values give indications on particle shape and/or surface roughness, i.e., S decreased with increased surface area due to shape deviation from sphericity and/or because of having rough instead of smooth surface.

Dissolution kinetics of the particle in the flowing water is described by Eq. (3) according to Fick's Law [9,11,29]:

$$\frac{dm}{dt} = -ka(C_S - C_b) \tag{3}$$

where m is particle mass (μg), t is dissolution time (min), k is mass transfer coefficient (cm/min), C_S is water solubility (mg/L), and C_b is bulk concentration beyond the stagnant layer boundary (mg/L). The particle mass, m, is determined by Eq. (4):

$$m = \rho V \tag{4}$$

where ρ is particle density (g/mL). At given temperature and flow rate, the mass transfer coefficient, k, is a constant [30]. Substituting Eqs. (1), (2), and (4) into Eq. (3) and simplifying, results in Eq. (5):

$$\frac{dr}{dt} = -\frac{k}{\rho S}(C_S - C_b) \tag{5}$$

In the present study, the values of C_b are much smaller than those of C_S (i.e., $C_b \ll C_S$). First, the flow velocities were high and the contact times between the flowing water and particles were short (<0.2 s). Second, the particles under study were situated in the upstream areas of the flow channels. They were thus subject to low bulk concentrations of the dissolved TNT, RDX, and HMX that accumulated from the dissolution of the front particles. Back calculations using the model parameters obtained with the method described in Section 3.3 did show that C_b values were <0.5% of C_S.

As such, the values of C_b were assumed to be negligible in comparison to C_S, which as was usually adopted in the literature [9,11,29], allowing $(C_S - C_b)$ in Eq. (5) to be simplified to C_S. By integration, the following analytical solution of Eq. (5) is thus obtained:

$$r = r_0 - \frac{kC_S}{\rho S}t \tag{6}$$

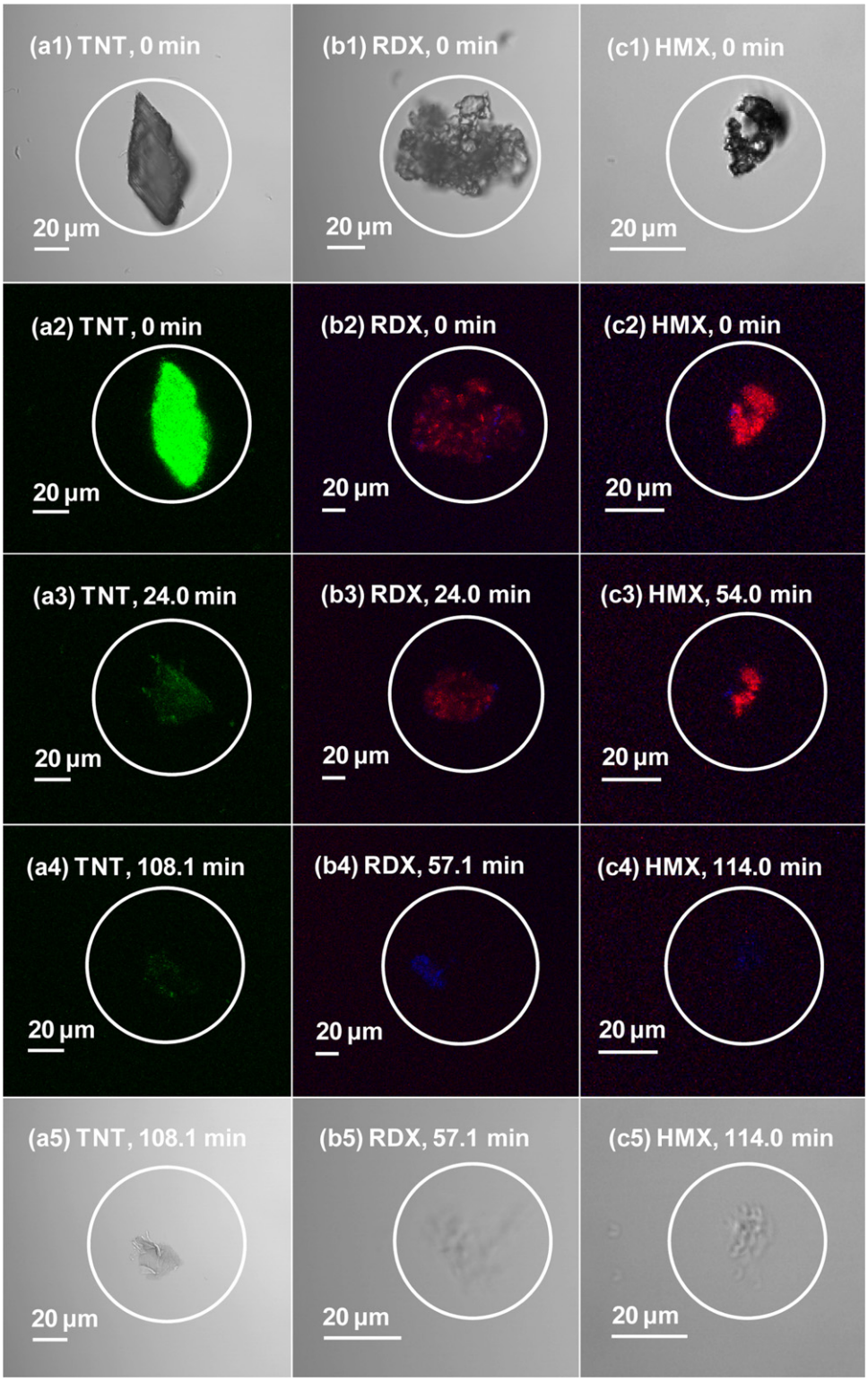

Fig. 1. Bright field and processed spectral images of individual (a1) to (a5) TNT, (b1) to (b5) RDX, and (c1) to (c5) HMX particles at the various dissolution times. Water flows from right to left.

where r_0 is initial radius (μm) of the perfect sphere which has the same volume as the real particle.

3.2. Model incorporating the resistance term

Eq. (6) indicates that the radius of the perfect sphere linearly decreases as the dissolution elapses. This, however, did not occur at the latter stages of TNT dissolution. The discrepancy is attributed to the resistance effect [9] caused by the unexposed surface areas of particles due to their attachment to channel surfaces.

In our test system (and, correspondingly, in the representative soil environment), a portion of the surface area of the explosive particle, a, in Eq. (3), may not be in contact with the aqueous phase, and thus not available for dissolution. The fraction of the unexposed

surface area can be negligible [e.g. in the case 1 of Fig. S1(b)] and dissolution proceeds as modeled by Eq. (3) (as well as the derived Eq. (6)). However, when the fraction of the unexposed surface area becomes significant [e.g., in the case 2 of Fig. S1(b)], the dissolution may be considerably reduced, and deviations from both Eqs. (3) and (6) are thus observed.

To take into account the resistance effect caused by the unexposed surface, a time-dependent function, $f(t)$, is incorporated into Eq. (3) as follows:

$$\frac{dm}{dt} = -k\,[1 - f(t)]\,aC_S \tag{7}$$

where $[1 - f(t)]$ is regarded as the fraction of exposed surface area that is in contact with the aqueous phase (and available for dissolution), and $f(t)$ is expressed as

$$f(t) = 1 - e^{-Rt} \tag{8}$$

where R is resistance coefficient (min^{-1}). A large R represents a big $f(t)$ and correspondingly a high fraction of unexposed surface area or equivalently a low fraction of exposed surface area, resulting in significant resistance effect. Eq. (8) is empirical, mainly due to the lack of theoretical geometric description of the fractional change of unexposed area during dissolution. Nevertheless, the equation proved useful and easy to use for the present applications (discussed below).

Substituting Eqs. (1), (2), (4), and (8) into Eq. (7) and simplifying yields Eq. (9):

$$\frac{dr}{dt} = -\frac{kC_S}{\rho S}e^{-Rt} \tag{9}$$

Integration of Eq. (9) leads to the following analytical solution:

$$r = r_0 - \frac{kC_S}{\rho SR}\left(1 - e^{-Rt}\right) \tag{10}$$

With the value of r on the left side of Eq. (10) determined, the values of a, V, and m can be obtained by applying Eqs. (1), (2), and (4), respectively. The specific surface area, A (m^2/g), can then be calculated with:

$$A = \frac{a}{m} \tag{11}$$

3.3. Fitting of the models

The calculated results according to Eq. (10) were fitted to the experimental data. A summary of all parameters that were used in the models is shown in Table 1. The parameters of ρ and C_S are constant at a given temperature (Table 1), whereas k, S, and R are fitting parameters and can be changed upon other factors. Because two of the three changeable parameters, i.e. k and S, can be lumped into one parameter expressed as k/S, it would be inappropriate to treat both as fitting parameters simultaneously. Since the S values were stable throughout the dissolution processes [Fig. 2(a4) to (c4)] and could be averaged from all measurements, the changeable parameters k and R were chosen as the fitting parameters.

The two fitting parameters were then determined by changing their values in a non-linear Excel solver (Microsoft Office Excel 2007) to reach the minimum sum of square error (SSE) between the model-calculated and experimental data [31]. Once the optimal values were determined, Eqs. (1), (2), (4), (10), and (11) were fully solved with the known parameter values (Table 1) and initial condition (r_0). The model-calculated values of r, a, V, m, and A were thereafter plotted for comparison to their respective experimental measurements.

For the purpose of comparison, Eq. (6) was also fitted with the experimental data using k as the fitting parameter. Eq. (6) represents the simple model based on Fick's Law without consideration of the resistance effect. Eq. (6) was fitted using the linear part of the experimental data. Similarly, after the value of r on the left side of Eq. (6) was obtained, the values of a, V, m, and A were calculated using Eqs. (1), (2), (4), and (11), respectively.

4. Results

4.1. TNT dissolution

Bright field images of an individual TNT particle at the beginning and end of the dissolution process are shown in Fig. 1(a1) and (a5), respectively. The size of the TNT particle significantly reduced as it dissolved [Fig. 1(a1) vs Fig. 1(a5)]. The processed spectral images [Fig. 1(a2) to (a4)] and Movie S1 show that the intensity of green fluorescence of TNT [25] decreased extensively over time. Because photo bleaching under the experimental conditions was minimal as has been discussed elsewhere [25], the decreasing intensity of green fluorescence of TNT is indicative of the ongoing dissolution process.

The changes of r, a, V, S, and A of the TNT particles as a function of time are demonstrated in Fig. 2(a1) to (a5). It is shown that the TNT radii decreased linearly before $t = 30$ min and thereafter the decrease became nonlinear [Fig. 2(a1)]. The TNT surface areas and volumes declined fast in the first 30 min and then decreased slowly [Fig. 2(a2) and (a3)]. Throughout the dissolution process, the shape factor curve was generally flat [Fig. 2(a4)]. The initial specific surface area of TNT was $0.94 \pm 0.03\ m^2/g$ [Fig. 2(a5)], much larger than the previous reported value of $0.0034 \pm 0.0008\ m^2/g$ [29]. There was a rapid increase in TNT specific surface area before $t = 30$ min and the value rose slowly thereafter [Fig. 2(a5)].

Fig. 2(a1) to (a5) shows that the model based on Fick's Law without consideration of the resistance effect (dash lines) accurately captured the experimental data (open circles) before $t = 30$ min. From 30 min onward, the model results deviated from the experimental measurements. In contrast, the model incorporating the resistance term (solid lines) fit the experimental data throughout the dissolution process very well ($R^2 > 0.90$ and $P < 0.0001$).

Furthermore, the calculated apparent mass transfer coefficient of TNT (defined as k/S) was 1.2 cm/min. This value was higher than the previously published values, which ranged from 0.023 to 0.14 cm/min [8,9,29]. The average shape factor was 0.068 (Table 1), and was much less than the value of 1.00 that would be expected for a perfect sphere.

4.2. RDX and HMX dissolution

Bright field images of RDX and HMX are presented in Fig. 1(b1) and (b5) and (c1) and (c5), respectively. It was observed that the RDX and HMX particles became almost invisible at the end of the dissolution process [Fig. 1(b5) and (c5)]. Previously, both RDX and HMX were reported to emit red and blue fluorescence [25]. The results from the present study confirmed those observations [e.g., Fig. 1(b3) and (c3)]. Moreover, Fig. 2(b2) to (b4) and Movie S2 and Fig. 2(c2) to (c4) and Movie S3 demonstrate that there was a large reduction in the overall florescent areas of both RDX and HMX as the time elapsed. Again, photo bleaching under the experimental conditions was minimal for RDX and HMX [25]; therefore, the decreasing florescent areas indicated the progressive dissolution of both RDX and HMX.

The changes of r, a, V, S, and A of the RDX and HMX particles as a function of time are demonstrated in Fig. 2(b1) to (b5) and (c1) to (c5), respectively. As shown, the radii (r) of RDX and HMX particles decreased linearly [Fig. 2(b1) and (c1)]; the surface areas and volumes of both RDX and HMX declined fast without an apparent slow-down stage [Fig. 2(b2) to (b3) and (c2) to (c3)]; and the shape factor curves of both RDX and HMX were

Table 1
Parameters and variables used in the dissolution model.[a]

Parameters and variables	Symbol	Value			Unit	Reference
		TNT	RDX	HMX		
Particle						
Surface area	a	Variable	Variable	Variable	μm^2	Measurement
Radius of a perfect sphere[b] with the same volume	r	Variable	Variable	Variable	μm	Calculation
Initial radius of a perfect sphere	r_0	25.8	24.5	9.1	μm	Calculation
Shape factor[c]	S	0.068	0.076	0.14	Dimensionless	Calculation
Volume	V	Variable	Variable	Variable	μm^3	Measurement
Mass	m	Variable	Variable	Variable	μg	Calculation
Density	ρ	1.65	1.82	1.90	g/mL	[32]
Specific surface area	A	Variable	Variable	Variable	m^2/g	Calculation
Dissolution						
Mass transfer coefficient	k	0.082	0.11	0.27	cm/min	Fitting
Solubility	C_S	116.6	40.2	3.6	mg/L	[21]
Bulk concentration	C_b	~0	~0	~0	mg/L	Assumption[d]
Resistance coefficient	R	4.72×10^{-2}	1.00×10^{-7}	2.71×10^{-7}	min^{-1}	Fitting

[a] Parameter means that it was a constant but not a function of time (t, min), whereas variable denotes that it was a function of time; the temperature was 22.0 °C.
[b] Perfect sphere is here defined as spherical particle with smooth surface.
[c] The shape factor was averaged from the experimental measurements in Fig. 2(a4) to (c4).
[d] The bulk concentration was assumed as low as almost zero (i.e., $C_b \ll C_S$) according to the discussion in Section 3.1.

flat [Fig. 2(b4) and (c4)]. The initial specific surface area of HMX was $1.21 \pm 0.24\ m^2/g$ [Fig. 2(c5)], much higher than the previous reported value of $0.012\ m^2/g$ [29]. Though the initial particle size of RDX [$24.4 \pm 1.8\ \mu m$ in Fig. 2(b1)] was larger than that of HMX [$9.1 \pm 0.9\ \mu m$ in Fig. 2(c1)], the initial specific surface area of RDX [$1.2 \pm 0.3\ m^2/g$ in Fig. 2(b5)] was almost equal to that of the HMX [$1.2 \pm 0.2\ m^2/g$ in Fig. 2(c5)].

Fig. 2(b1) to (b5) and (c1) to (c5) further shows that both the model based on Fick's Law without consideration of the resistance effect (dash lines) and the model incorporating the resistance term (solid lines) described the experimental data (open circles) quite well ($R^2 > 0.77$ and $P < 0.0001$). In addition, the calculated apparent mass transfer coefficient (k/S) of HMX was 1.9 cm/min, which is higher than the previously reported values from 0.035 to 0.75 cm/min [8,9,29]. The average shape factors of RDX and HMX were 0.076 and 0.14, respectively, much smaller than the value of a perfect sphere of 1.00.

5. Discussion

The nearly flat shape factor curves for TNT, RDX, HMX [Fig. 2(a4) to (c4)] suggested that the shapes and surface roughness of individual particles might be unchanged overall during the dissolution processes. The observations were similar to our previous report [25] that the shape factors of microscale Composition B residues did not change much during dissolution. The values of the shape factors of TNT, RDX, and HMX were much less than 1.00 (Table 1), indicating that the crystals of TNT, RDX, and HMX had very non-spherical shapes and perhaps also possessed very rough surface due to the attachment of some tiny crystals [Fig. 1(b1) and (c1)]. This implies that it is important to incorporate a shape factor in Eq. (1) to obtain improved modeling accuracy.

The quick increase in the specific surface area at the early stage of TNT dissolution [Fig. 2(a5)] was mainly attributed to the quickly decreasing particle size [Fig. 2(a1)]. The larger specific surface areas of TNT and HMX than the previous reports were most likely because of the smaller particle sizes (tens of μm) used in the present study than in the literature (~several mm). Also, it was likely that the non-spherical shape or the rough surface might be partially responsible because the particles were most likely assumed to be spherical or smooth in the previous reports [29]. The observation that the RDX had a larger particle size than the HMX, but possessed a similar specific surface area, indicates that the RDX particles might be more irregular in shape and/or much rougher on surfaces in comparison to the HMX particles. This conclusion was also supported by their relative shape factors, 0.076 of RDX vs 0.14 of HMX, shown in Table 1.

The deviations between the predicted and experimental measurements of TNT dissolution at later times suggested that the model based on Fick's Law and without consideration of the resistance effect was not valid to describe the dissolution processes of TNT. Conversely, the model incorporating the resistance term captured the experimental data of individual TNT, RDX, and HMX throughout the dissolution processes very well, indicating that this model was more robust. Thus, Eqs. (7) and (8), developed from the latter model, would be more appropriate for incorporation into a general model for describing the dissolution of mixed energetic residues.

Surface attachment seems to be more important in controlling the dissolution of TNT than that of RDX and HMX. This is likely because TNT's linear shapes [Fig. 1(a1)] gave rise to larger fraction of unexposed surface area due to attachment, whereas RDX and HMX were oblong [Fig. 1(b1) and (c1)] and led to smaller or even negligible fractions of unexposed surface area under the experimental conditions. Apparently, the resistance effect is reflected only important to TNT in the present study.

The observation of the resistance effect due to surface attachment implies that, when microscale energetic residues, such as Tritonal (TNT/aluminum: 80/20), Composition B (RDX/TNT/wax: 60/39/1), and Octol (HMX/TNT: 70/30) [8], migrate into soil systems and attach to soil grains, their dissolution rates are likely to be lower than their unattached counterparts. Under such circumstances, longer duration of the spreading of explosive compounds from the particles' dissolution might occur in the contaminated soil systems.

The apparent mass transfer coefficients (k/S) obtained in this study were higher than the previously reported values, most likely because of the much higher flow rates used in the present study. Interestingly, the acquired mass transfer coefficients (k) followed the order of TNT < RDX < HMX, which is in contrast to the solubility order of TNT > RDX > HMX (Table 1), suggesting that compounds with high solubility may have low mass transfer coefficients. In the meantime, assuming that the surface areas of TNT, RDX, and HMX were all $1.0\ m^2$, according to Eq. (3) and Table 1 the calculated dissolution flux [$dm/(a \cdot dt)$] of TNT, RDX, and HMX during the initial dissolution stage would be 0.96, 0.44, and 0.097 mg/(m^2 min), respectively. These results suggest that the TNT dissolved much faster than RDX and HMX, consistent with the general knowledge and implying that the newly developed spectral imaging method [25] could be reliable.

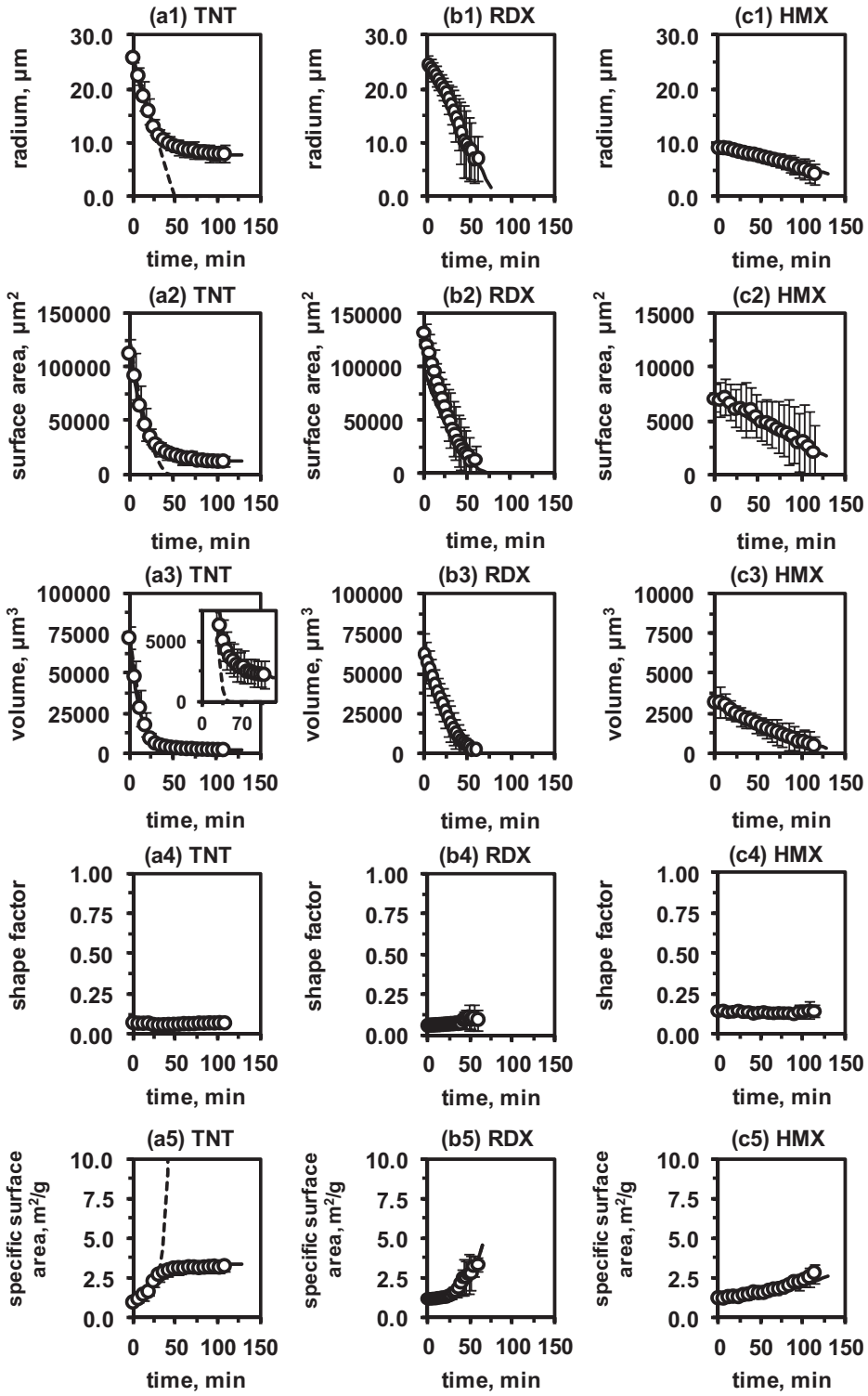

Fig. 2. Quantification and modeling of the dissolution of individual (a1) to (a5) TNT, (b1) to (b5) RDX, and (c1) to (c5) HMX particles. Open circles represent the experimental data that are the average of triplicate measurements; error bars show the standard deviation; dash lines are the model-calculated results based on Fick's Law without consideration of the resistance effect; solid lines are the model-calculated results incorporating the resistance term.

6. Conclusions

The dissolution of crystals (<100 μm) of individual TNT, RDX, and HMX under continuous flow conditions was investigated. A newly developed spectral imaging method was applied to observe and quantify the dissolution processes in micromodel channels. Dissolution models were thereafter developed to describe the changes of radii, surface areas, volumes, and specific surface areas of those individual energetic particles as a function of time. The following conclusions were drawn based on the experimental and modeling results:

(1) Surface attachment of explosive particles on channel surfaces could be important in controlling the particles' dissolution

when the fraction of unexposed surface area was high due to the surface attachment. This implies that in contaminated soil systems, attached explosive particles may serve as long-term sources for spreading of explosive compounds from the particles' dissolution.

(2) A model incorporating a resistance term that takes into account unexposed surface area was found to accurately describe the dissolution of TNT, RDX, and HMX under continuous flow conditions. The developed model laid a foundation for the further development of a general modeling approach to capture the dissolution of mixed energetic residues.

(3) The spectral imaging method provides a new pore-scale technique for mass transfer investigation of TNT, RDX, and HMX, which provides mechanistic insight and is complementary to batch and column studies. The measured mass transfer coefficients in the present study followed the order of TNT < RDX < HMX.

Acknowledgments

This project was supported by the US Strategic Environmental Research and Development Program (SERDP) under contract W912HQ-09-C0012 and by the NSF Delaware EPSCoR (Experimental Program to Stimulate Competitive Research) Research Infrastructure Improvement Program (RII-2) grant. We thank Dr. Kirk Czymmek for helping the emission spectra measurement, Dr. Stephen Fallis (Naval Air Warfare Center Weapons Division, China Lake) for providing the suspensions of individual TNT, RDX, and HMX, and Michael Doody for revising the manuscript. Views, opinions, and/or findings contained in this report are those of the author(s) and should not be construed as an official Department of Defense position or decision unless so designated by other official documentation.

Appendix A. Supplementary data

Supplementary data associated with this article can be found, in the online version, at doi:10.1016/j.jhazmat.2012.03.012.

References

[1] A.D. Hewitt, S.R. Bigl, Elution of Energetic Compounds from Propellant and Composition B Residues, Engineer Research and Development Center, Cold Regions Research and Engineering Laboratory, Hanover, New Hampshire, USA, 2005.
[2] Agency for toxic substances and disease registry (ATSDR) toxic substances portal – RDX (2010): http://www.atsdr.cdc.gov/toxfaqs/tf.asp?id=411&tid=72#bookmark02.
[3] ATSDR toxic substances portal – HMX (1997): http://www.atsdr.cdc.gov/ToxProfiles/tp98.pdf.
[4] ATSDR toxic substances portal – TNT (1996): http://www.atsdr.cdc.gov/toxfaqs/tf.asp?id=676&tid=125.
[5] USEPA drinking water health advisories (2006): http://water.epa.gov/action/advisories/drinking/dwstandards.cfm.
[6] A.M. Jaramillo, T.A. Douglas, M.E. Walsh, T.P. Trainor, Dissolution and sorption of hexahydro-1,3,5-trinitro-1,3,5-triazine (RDX) and 2,4,6-trinitrotoluene (TNT) residues from detonated mineral surfaces, Chemosphere 84 (2011) 1058–1065.
[7] K.M. Dontsova, S.L. Yost, J. Simunek, J.C. Pennington, C.W. Williford, Dissolution and transport of TNT, RDX, and Composition B in saturated soil columns, J, Environ. Qual. 35 (2006) 2043–2054.
[8] S. Taylor, J.H. Lever, J. Fadden, N. Perron, B. Packer, Simulated rainfall-driven dissolution of TNT, Tritonal, Comp B and Octol particles, Chemosphere 75 (2009) 1074–1081.
[9] J.C. Lynch, J.M. Brannon, K. Hatfield, J.J. Delfino, An exploratory approach to modeling explosive compound persistence and flux using dissolution kinetics, J. Contam. Hydrol. 66 (2003) 147–159.
[10] J.S. Furey, H.L. Fredrickson, M.J. Richmond, M. Michel, Effective elution of RDX and TNT from particles of Comp B in surface soil, Chemosphere 70 (2008) 1175–1181.
[11] J.C. Lynch, J.M. Brannon, J.J. Delfino, Dissolution rates of three high explosive compounds: TNT, RDX, and HMX, Chemosphere 47 (2002) 725–734.
[12] M.C. Morley, H. Yamamoto, G.E. Speitel, J. Clausen, Dissolution kinetics of high explosives particles in a saturated sandy soil, J. Contam. Hydrol. 85 (2006) 141–158.
[13] J.H. Lever, S. Taylor, L. Perovich, K. Bjella, B. Packer, Dissolution of composition B detonation residuals, Environ. Sci. Technol. 39 (2005) 8803–8811.
[14] M.E. Walsh, S. Taylor, A.D. Hewitt, M.R. Walsh, C.A. Ramsey, C.M. Collins, Field observations of the persistence of Comp B explosives residues in a salt marsh impact area, Chemosphere 78 (2010) 467–473.
[15] A.D. Hewitt, T.F. Jenkins, M.E. Walsh, M.R. Walsh, S. Taylor, RDX and TNT residues from live-fire and blow-in-place detonations, Chemosphere 61 (2005) 888–894.
[16] S. Taylor, J.H. Lever, J. Fadden, N. Perron, B. Packer, Outdoor weathering and dissolution of TNT and Tritonal, Chemosphere 77 (2009) 1338–1345.
[17] J.C. Pennington, B. Silverblatt, K. Poe, C.A. Hayes, S. Yost, Explosive residues from low-order detonations of heavy artillery and mortar rounds, Soil Sediment Contam. 17 (2008) 533–546.
[18] S. Taylor, A. Hewitt, J. Lever, C. Hayes, L. Perovich, P. Thorne, C. Daghlian, TNT particle size distributions from detonated 155-mm howitzer rounds, Chemosphere 55 (2004) 357–367.
[19] S. Taylor, E. Campbell, L. Perovich, J. Lever, J. Pennington, Characteristics of Composition B particles from blow-in-place detonations, Chemosphere 65 (2006) 1405–1413.
[20] J.C. Lynch, J.M. Brannon, J.J. Delfino, Effects of component interactions on the aqueous solubilities and dissolution rates of the explosive formulations octol, composition B, and LX-14, J. Chem. Eng. Data 47 (2002) 542–549.
[21] J.C. Lynch, K.F. Myers, J.M. Brannon, J.J. Delfino, Effects of pH and temperature on the aqueous solubility and dissolution rate of 2,4,6-trinitrotoluene (TNT), hexahydro-1,3,5-trinitro-1,3,5-triazine (RDX), and octahydro-1,3,5,7-tetranitro-1,3,5,7-tetrazocine (HMX), J. Chem. Eng. Data 46 (2001) 1549–1555.
[22] K.S. Ro, A. Venugopal, D.D. Adrian, D. Constant, K. Qaisi, K.T. Valsaraj, L.J. Thibodeaux, D. Roy, Solubility of 2,4,6-trinitrotoluene (TNT) in water, J. Chem. Eng. Data 41 (1996) 758–761.
[23] J.M. Phelan, J.L. Barnett, Solubility of 2,4-dinitrotoluene and 2,4,6-trinitrotoluene in water, J. Chem. Eng. Data 46 (2001) 375–376.
[24] C.A. Taylor, W.H. Rinkenbach, The solubility of trinitrotoluene in organic solvents, J. Am. Chem. Soc. 45 (1923) 44–59.
[25] C. Wang, V. Lazouskaya, M.E. Fuller, J.L. Caplan, C.E. Schaefer, Y. Jin, Dissolution of microscale energetic residues in saturated porous media: visualization and quantification at the pore-scale by spectral confocal microscopy, Environ. Sci. Technol. 45 (2011) 8352–8358.
[26] Zeiss online tutorial – spectral imaging with linear unmixing (2010): http://zeiss-campus.magnet.fsu.edu/tutorials/spectralimaging/linearunmixing/index.html.
[27] Zeiss online tutorial – introduction to spectral imaging and linear unmixing (2010): http://zeiss-campus.magnet.fsu.edu/articles/spectralimaging/introduction.html.
[28] PerkinElmer volocity user guide (2010): http://www.cellularimaging.com/pdfs/manuals/VolocityUserGuide.pdf.
[29] F. Monteil-Rivera, S. Deschamps, G. Ampleman, S. Thiboutot, J. Hawari, Dissolution of a new explosive formulation containing TNT and HMX: comparison with octol, J. Hazard. Mater. 174 (2010) 281–288.
[30] S.W. Webb, J.M. Phelan, T. Hadgu, J.S. Stein, C.M. Sallaberry, Measurement and modeling of energetic-material mass transfer to soil-pore water – Project CP-1227 Final Technical Report, Sandia National Laboratories, Albuquerque, New Mexico and Livermore, California, USA, 2006.
[31] C. Wang, L. Lippincott, X. Meng, Kinetics of biological perchlorate reduction and pH effect, J. Hazard. Mater. 153 (2008) 663–669.
[32] D.M. Townsend, T.E. Myers, Recent Developments in Formulating Model Descriptors for Surface Transformation and Sorption of TNT, RDX, and HMX, US Army Corps of Engineers, Waterways Experiment Station, Vicksburg, Mississippi, USA, 1996.